Chapter 6

Image reconstruction model formulation and approximation

In this Chapter we deal with the B-mode imaging model and we propose to approximate the reconstructions provided by the classical Delay and Sum algorithm (DAS) by means of deconvolution process.

DAS is a fundamental signal processing technique widely used in various applications, particularly in the field of acoustics and ultrasound imaging, specifically employed for beamforming signals received by an array of sensors. Essentially, the DAS operates by introducing controlled delays to the signals received by individual sensors within an array and then summing these delayed signals. By tuning the delays appropriately, the algorithm can steer the combined signal in a specific direction, thus forming a focused beam. The primary objective of the DAS is to improve the signal-to-noise ratio and enhance the detection and localization of a desired signal while suppressing unwanted noise and interference from other directions. The simplicity and effectiveness of the Delay and Sum algorithm makes it a popular choice in real-time applications where quick and accurate spatial filtering of signals is crucial. The goal of this chapter is to describe how to approximate the DAS algorithm as a deconvolution process: in order to do so we first describe the DAS algorithm as a time convolutional-like model where the point spread

function (PSF) depends on the delays, which, in their term, depend on time. Our approximation is then based on time-independent delays and provide a local invariant formulation that can signicantly reduce DAS computational costs.

6.1 Receiving phase and dynamic focusing model

We proceed by describing in our notation DAS algorithm for the classical B-mode ultrasound images. A single image is obtained performing several acquisitions and consists in building the image synthetically focalizing the emitted and received ultrasound. For one focused transmission a slice of the image is reconstructed by summing ad weighting many recorded signals. The image obtained is an extimation of the tissue reflectivity function, which measures the ability of the body to reflect ultrasounds signals, as described in Chapter 3.

The signal recorded by the probe is the pressure wave scattered back from the cells in the body. As for transmission, the reflected ultrasound propagates from the field to the probe and hits the piezoelectric elements. The active ones record a signal in time which was attenuated by the body, and have the same impulse response function of the transmission phase and is proportional to the reflectivity function of the body. The mathematical descrition of this set of phenomena is given in section 3.5.2 and 3.5.3 of the thesis. According to this description we suppose the body has a medium density level and the pressure waves propagates with a medium velocity. When the pressure wave crosses the cells, their density and velocity vary slightly, the tissue reflectivity function represents in each point this variation.

We denote by $N := \left[-\overline{N}, \cdots, \overline{N}-1\right]$ the subset of active elements symmetrical with respect to the probe center and $\gamma(\vec{r})$ the value of tissue reflectivity function in a field point $\vec{r}$. According to Chapter 4, we denote by $S_D^F(\vec{r},\cdot)$, defined in eq. (4.4), the transmitted signal focused in $\vec{F}$ that crosses the point $\vec{r}$. The pressure wave scattered back from the point hits all the active elements,

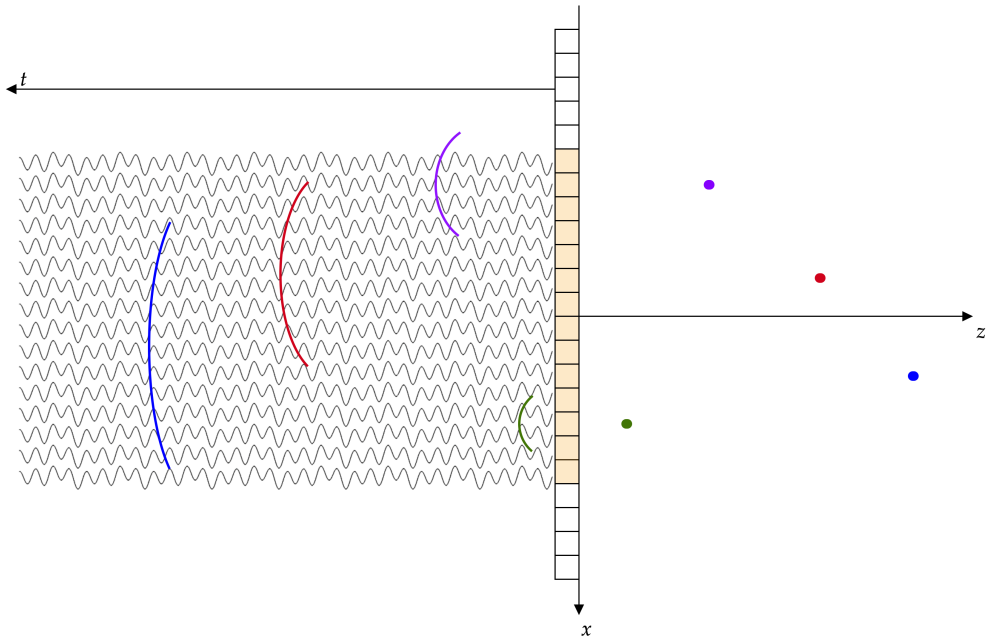

Figure 6.1: Picturing of how signals are recorded and how the delays interact with them to dynamic focus them. After having applyied the correct delays curve, the selected samples are summed together to estimate the corresponding pixel intensity

and thus we have a collection of recorded signals:

$$S_n^F(\vec{r},\cdot) = \gamma^\dagger(\vec{r}) S_D^F(\vec{r},\cdot) * H_n(\vec{r},\cdot) \quad \forall n \in N, \tag{6.1}$$

where $H_n(\vec{r},\cdot)$ defined in eq. (4.1) is the same attenuated impulse response as the signal undergoes the same attenuation, as it depends only on the trajectory, and N is the subset of active elements on the probe. In general, we do not have a single scattering point but a collection of them, all scattering back the transmitted signal. Relying on Born's approximation, then discarding the second order effects, as described in eq. (3.23), we consider the contribution given by the mutual interaction of the scattered waves to be negligible. With reference to section 2.5, we can state the recorded signal is the sum of all the

waves reflected in the field Ω:

$$S_n^F = \sum_{\vec{r}\in\Omega} \left[S_D^F(\vec{r}, \cdot) * H_n(\vec{r}.\cdot) \right] \gamma^{\dagger}(\vec{r}) \tag{6.2}$$

B-mode images are usually obtained recombining the signals with the Delay and Sum Algorithm [56], whose basic principle is that the signal emitted from a single point hits different active elements of the probe at different times. The algorithm performs the dynamical focusing by applying a different delay curve for each point to be reconstructed, as displayed in Figure 6.1. The differences in time of flight are exploited by summing together distinct signals samples for each pixel. Thus, the value of tissue reflectivity function in a fixed point is estimated as:

$$\gamma(\vec{r}) = \sum_{n\in N} S_n^F * \delta_{D_n(\vec{r})} \tag{6.3}$$

As for transmission phase, we can introduce a multiplicative weight $A_n(\vec{r}) \in \mathbb{R}$ accounting for the *importance* of each active element. The rationale is the more the point is aligned with an element, the less the received signal is attenuated or affected by noise whereas if the trajectory is longer, the signal strength is reduced due to attenuation and the signal-to-noise ratio decreases. Formally, each pixel will be reconstructed as follows:

$$\gamma_A(\vec{r}) = \sum_{n\in N} A_n(\vec{r}) S_n^R * \delta_{D_n(\vec{r})}. \tag{6.4}$$

Hereafter, we neglect this multiplicative weights, i.e. the apodizated form of the reconstructions, and we will analyze the effects of delays on the PSF.

6.1.1 Single scatterer case

We focus on the case of single scatterer and describe th PSF formulation model. Thus, we consider to have a single scatterer in a point $\vec{r}$ that reflects the echo in $\vec{r}$ whereas the transmission is focused in $\vec{F}$. The signal received by the element

n is:

$$S_n^{F,\vec{r}}(t) := \left(H_j^{\vec{r}} * S^{F,\vec{r}}\right)(t). \tag{6.5}$$

The coresponding reconstructed value is:

$$\gamma^{\vec{r}} = \sum_{n \in N} S_n^{F,\vec{r}} * \delta_{D_n^{\vec{r}}}. \tag{6.6}$$

It is clear from the formulation that although the product in eq 6.6 takes the form of a convolution, the candidate PSF depends on time, as the delays $D_n^{\vec{r}}$ do. Thus, we introduce a local approximation of the delays to write the reconstruction formula as a convolution, valid in a neighborhood of F. Our analysis is restricted to the line along the geometrical center of a linear probe.

6.2 Geometrical considerations about receiving delays

We proceed in describing how the number of active elements and the delays are usually computed.

6.2.1 Active surfaces computation

We report the most common criteria to compute the number of active elements depending on the depth of the target point. We introduce the *focal number criterium*, that can be used both in transmission and in receiving phase, and the *Kossof criterium* usually adopted in transmission phase. We can observe that:

- the deeper the focus, the greater the number of elements needed to reach it,
- the back-scattered signal will be more attenuated along depth, so it is reasonable to increase the number of the receiving elements.

Definition 4. *The focal number is the ratio between the depth of the returning echo divided by the active aperture of the probe:*

$$\phi = \frac{z}{A}, \tag{6.7}$$

where z is the depth we are considering and A is the active surface.

Consequently, by choosing a focal number and fixing a single depth of interest is possible to calculate the corresponding appropriate active surface. In transmission phase it is possible to use the Kossoff criterium [49]. If we fix a focalizing depth z_F, we can estimate the transmission active aperture as:

$$\mathcal{M}_T = \sqrt{\frac{3z_F\lambda}{k_f}}, \quad \text{where} \quad \begin{cases} k_f \geq \frac{1}{2}\pi & \text{weak focusing} \\ \frac{1}{2} \leq k_f \leq \frac{1}{2}\pi & \text{medium focusing} \\ k_f \leq \frac{1}{2} & \text{strong focusing} \end{cases} \tag{6.8}$$

where λ is the wavelength of the emitted signal and z is the depth of focus. We know the emitted field is focalized in a single point and results in an hourglass-shaped field, the Kossoff parameter k_f adjusts the axial intensity level of the emitted beam then adjusts how tight is the shape in the focal point [22, 53].

Clearly, in receiving phase the active surface increases with the depth. Thus, fixing a focal number f we have:

$$\mathcal{N}(z) = \frac{z}{\phi}.$$

Furthermore, the active aperture is limited by the structural properties of the probe. Then, $\mathcal{N}_R(z)$ is upper bounded by the length of the probe so that when it reaches the maximum values it remains constant in time (Fig. 6.2).

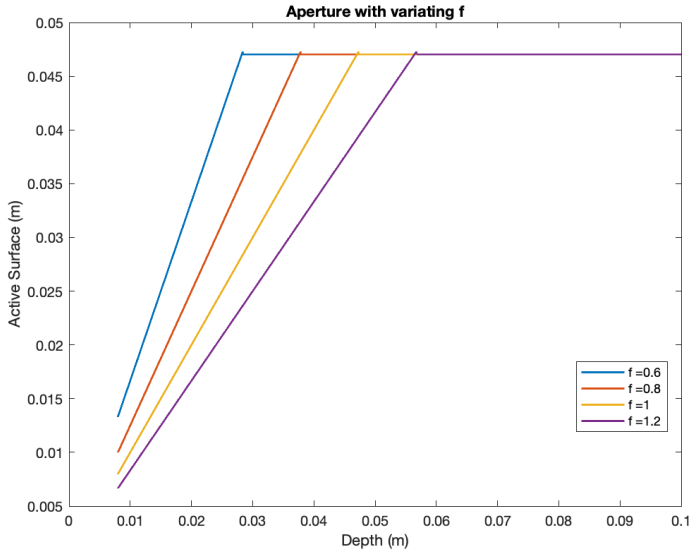

Figure 6.2: The figure represents how the active aperture in receiving varies in depth. The values are computed by using four different focal number and considering a linear probe with a maximum length of $0.047\,m$.

6.2.2 Receiving delays

As we have done in Chapter 2 in eq (2.2), we identify each active element with its geometrical center. Coherently on how we have defined the field, each element center will be $\vec{x}_n = (x_n, 0)$. In Figure 6.3 we compute several delay curves, corresponding to a dense sampling of the field space. Furthermore, having fixed the image plane to be $y = 0$, the targets point will have coordinate $\vec{r} = (x, z)$. As we focus on the central line, our target point is $\vec{r} = (0, z)$. With these assumptions, the delay corresponding to point-element pair is:

$$D_n(z) := \frac{1}{c}\left(z - \sqrt{x_n^2 + z^2}\right), \tag{6.9}$$

where c is the speed of sound across the field.

From a geometrical point of view, computing the delay curve for a point leads to estimate a parabola. The fact that each point $\vec{r}$ provides a differently shaped curve is encoded in the dependence on z of eq. (6.9). It is reasonable to

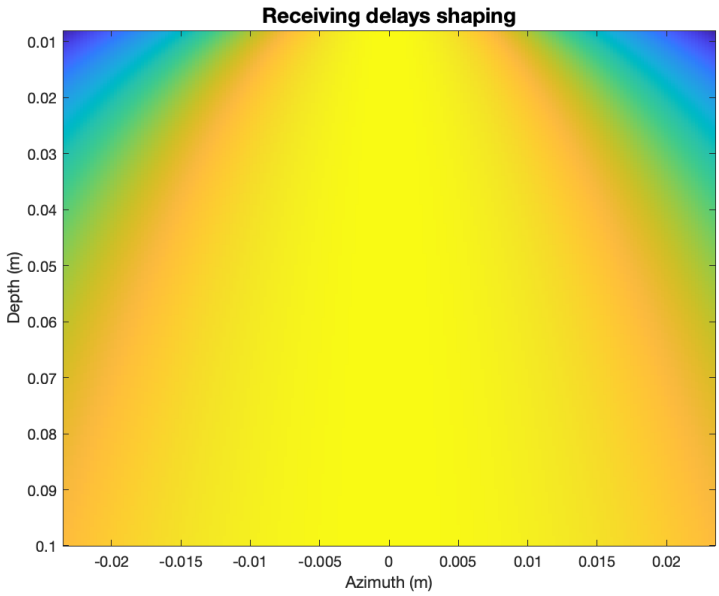

Figure 6.3: Picturing of all the delays curve obtained for a linear probe of 192 elements making the depth vary between $1cm$ and $10cm$. The image points out how the variation is smooth even discarding the fact that usually nearby the probe not all the elements are active.

expect the delays vary smoothly with respect to the depth, with the following remarks (ref. to Figure 6.4):

- the closest to the probe the less elements are active,
- the farther from the probe the higher is the flattening of the curve, thus reducing the variation between the curves.

It is possible to notice the slow variation of the delay curves. With reference to Figure 6.5, representing the curves for a limited set of depths, it becomes clear that the differences are smaller compared near the vertex to those along the tails. Additionally, it is noteworthy to observe that the variances are more pronounced in regions where the apodization weights are lower in standard weighted reconstruction.

Here we perform a brief analysis of the variation of the delays shapes in order to quantitatively assess the godness of the depth invariant assumption.

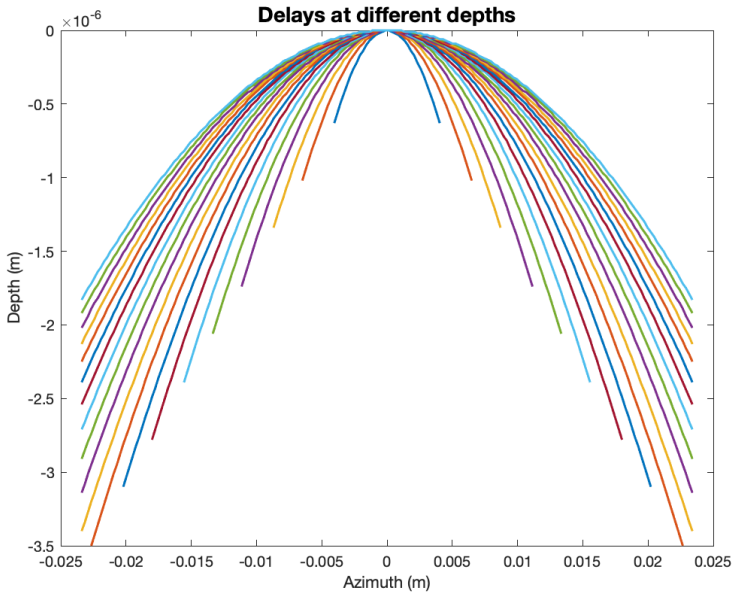

Figure 6.4: We display different delays curves used to reconstruct points at different depths. For each depth, we take in account also the different aperture estimated by the focal number rule, with focal number set to 1. The farther the target point is from the probe surface the higher is the flattening of the curve.

Such approximation allow us to write the model as a convolutional one and simplify the estimation of the PSF, which becomes time variant. We check that the variation at each depth is lower nearby the vertex and decreases with depth.

We fix a certain depth z_0 and we consider a neighborhood of depths $I_{z_0} = [z_0 - \epsilon, z_0 + \epsilon]$. Computing first order Taylor's expansion of eqn. 6.9, we get:

$$D_n(z) \simeq D_n(z_0) + \left.\frac{\partial D_n}{\partial z}\right|_{z_0} (z - z_0)$$

Leading to:

$$\frac{D_n(z) - D_n(z_0)}{D_n(z_0)} \simeq -\frac{1}{\sqrt{x_n^2 + z_0^2}}(z - z_0) \tag{6.10}$$

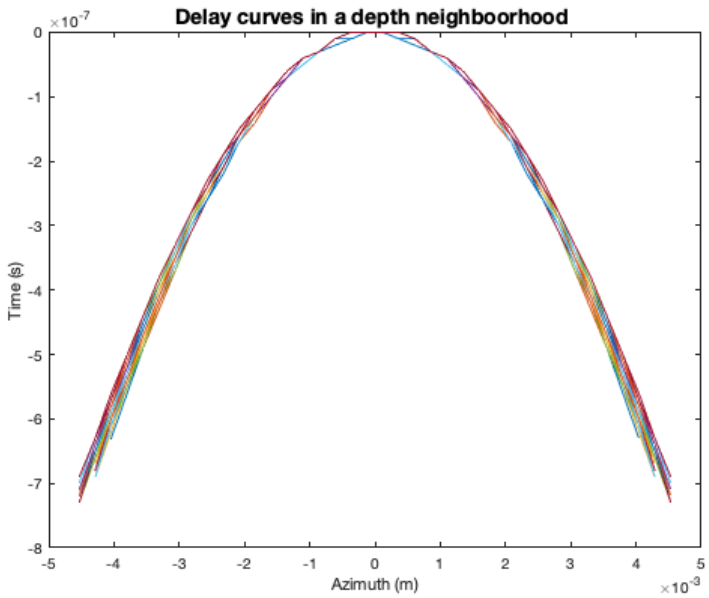

Figure 6.5: The graph displays many delay curves in the neighborhood of a target point. It is clear nearby the vertex the differences are smaller then along the tails. It is also worthable noticing the differences are higher where in standard DMAS reconstruction the apodization weights are lower.

We have

$$\frac{1}{\sqrt{x_n^2 + z_0^2}} \leq \frac{1}{z_0}.$$

Thus, in a neighborhood of depths, the relative difference between two delay curves decrease:

1. when we are looking at values on the tails, i.e. x_n increases;
2. when z_0 increases.

6.3 Empirical results on local delays invariance

As shown in the previous section, it seems reasonable that if the scatterer is in a neighborhood of the focal point we can apply constant the delay curve to reconstruct the tissue reflectivity function in a neighborhood of z_0

along the central line. In this section we numerically evaluate the validity of this assumption and then we formulate a local approximation of the DAS algorithm.

From now on, we will refer to one dimensional PSF as our reconstruction will be performed only on the central line of the field. To simulate the process, we have developed a Python code based on parUST [71].

In Figure 6.6 we display three different reconstructions. These three lines has been obtained by applying eq. (6.6) to signals simulated in each case, obtained by adding a single scatterer with reflectivity imposed to 1 in an homogeneous field. After having applied DAS algorithm, we compute the modulus of the signal and we have normalized the three reconstructions with respect to the maximum value of the second reconstruction (displayed in orange). It is worth noticing that the three lines seem to have very similar gaussian shapes that differ the most only at the bottom.

Our guess is that reconstructions of the tissue reflectivity function of a single scatterer, i.e. the PSFs of the imaging system, produced by the scattering from different points $\vec{r}$ along the central axis, mainly differ by their heights or the height of their peaks. The idea is that differences between PSFs can be dumped by introducing a multiplicative factor.

We start by validating our claim empirically. It is known that the point with the best reconstruction is the one at the transmit focal depth. Thus, we evaluate how much different are two reconstructions if performed with the delays corresponding to that point, i.e. the DAS delays, or with the delays for the focal point.

We performe the experiments according to the following settings:

- we consider a set of 600 scattering positions $\vec{r}$ in the range from $0.002\,m$ to $0.042\,m$, uniformly sampled;
- we consider a linear probe of 192 elements with $0.245\,mm$ pitch and $5\,mm$ height;
- we consider a Gaussian-modulated sinusoidal pulse in transmission with

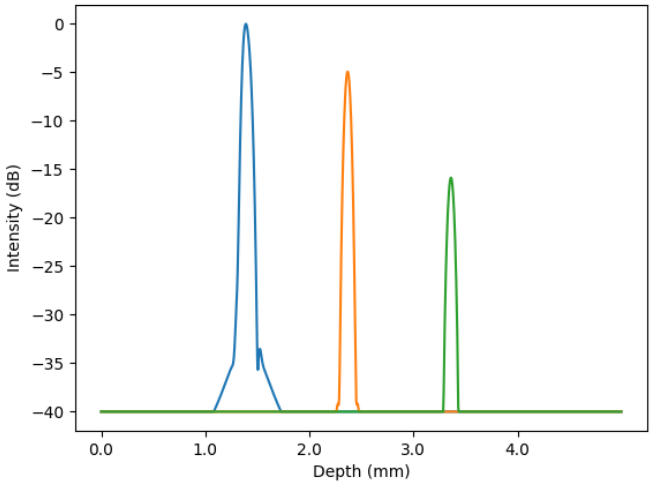

Figure 6.6: Different reconstruction of 1D PSF along the central line. Each color represents a reconstruction obtained in the case of just one scatterer present in the field. To display them together we have normalized all the values with respect to the maximum value of the blue one.

central frequency of $4, 5, 6, 7, 8, 9$ and $10\,MHz$,

- we consider two different Kossof parameters $k_f = 0.6, 0.8$ to establish the transmission active surface and focal number 1.2 to establish the receiving active surface;
- we do not introduce any steering;
- we consider three possible different focal points at $0.015, 0.025, 0.035\,m$ in depth.

Thus, we have 600 possible positions in $7 \cdot 2 \cdot 3 = 42$ different configurations by choosing differently central frequencies, Kossoff parameters and focal depths. In each setting, for each point, we perform two reconstructions assuming to have just a scatterer in the current point:

1. $\gamma(\vec{r})$ the recostruction obtained by applying the classical DAS algorithm,

2. $\hat{\gamma}(\vec{r})$ the reconstruction obtained by applying the delays of the focal point to signals scattered from $\vec{r}$.

We will refer to γ as the *standard* reconstruction and to $\hat{\gamma}$ as the *approximated* one. Thus, in each setting, if $\vec{r_F}$ is the transmission focal point, we have that $\gamma(\vec{r}) = \hat{\gamma}(\vec{r_F})$. To experimentally evaluate the error between the 600 reconstructions and evaluate the differences of each pair of reconstructions, we compute:

1. the Wasserstein distance of each pair, encoding how much distant are the two functions as energy distributions,
2. the absolute difference between the Full Width at Half Maximum (FWHM) of the two reconstructions,
3. the ratios between the peak of $\gamma(\vec{r})$ and $\hat{\gamma}(\vec{r})$.

Obtained results are displayed in Figures 6.7 6.8. These Figures include experiments with different k_f and display all the computed metrics for different choices of central frequency and focal point (indicated by the blue vertical line). We can observe some main trends:

1. the largest Wasserstain distance between pairs is about of order 10^{-4},
2. the approximated reconstructions have at most the same peak height of the standard ones in a neighborhood of the focus,
3. the FWHM differences are always less than 1 μm.

In all the graphs of the two figures, we have highlighted a box to identify a suitable neighborhood in which our approximation should be reasonable. In particular, there is a neighborhood of $\vec{r_F}$ where the Wasserstain distance and the FWHM are small enough so that a suitable rescaling factor applied to $\hat{\gamma}(\vec{r})$ well approximate the curve $\gamma(\vec{r})$. The oscillating behaviour in the measure could be mostly attributed to high number of pixels in the row that oversamples the field space.

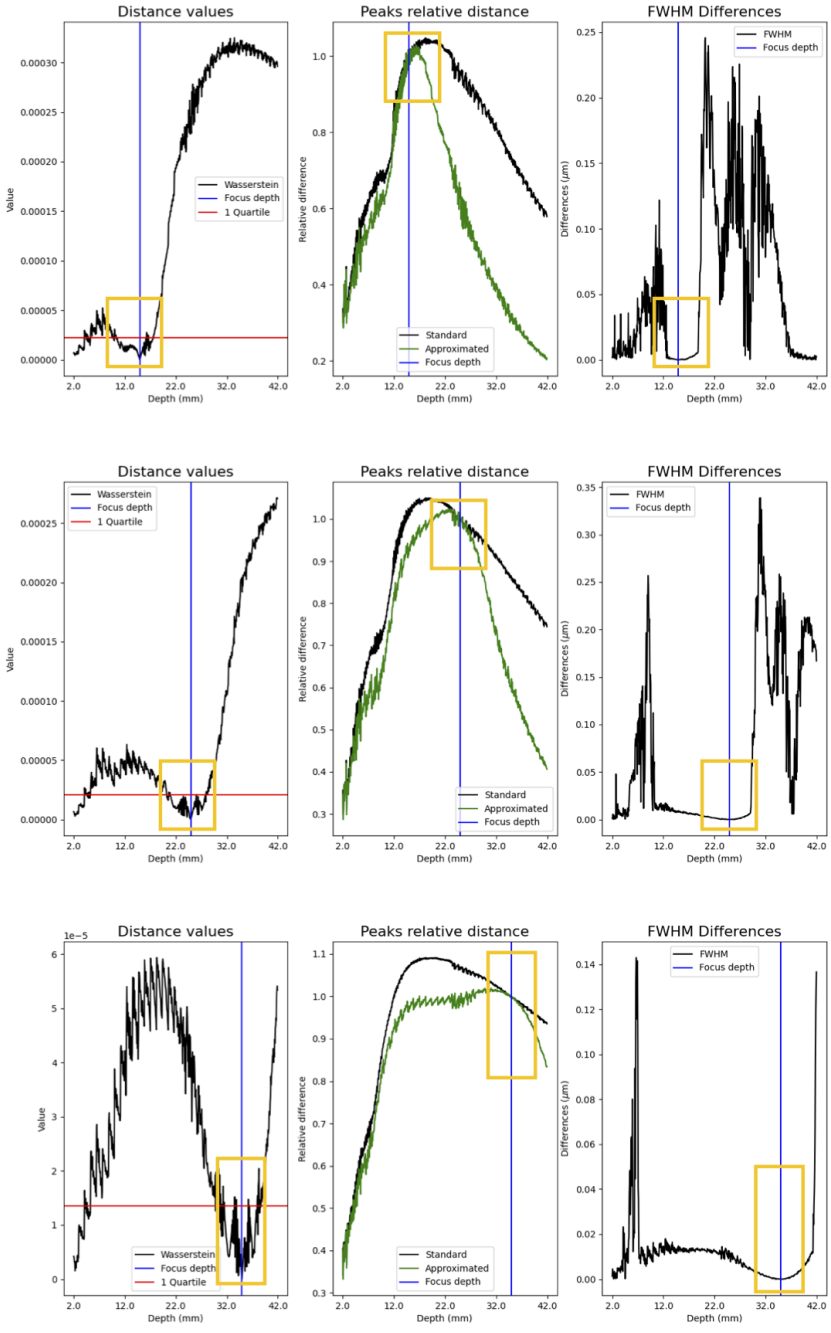

Figure 6.7: Fixing $k_f = 0.6$, each row shows the results for differerent focal points in increasing order. Moreover, to vary the most the differences of solutions, we have chosen a different frequency for each row, $9, 7, 5\,MHz$ respectively. Each of the three plot represents the Wasserstain distance, the peaks absolute difference and the FWHM differences respectively. The yellow box underline a possible neighborhood.

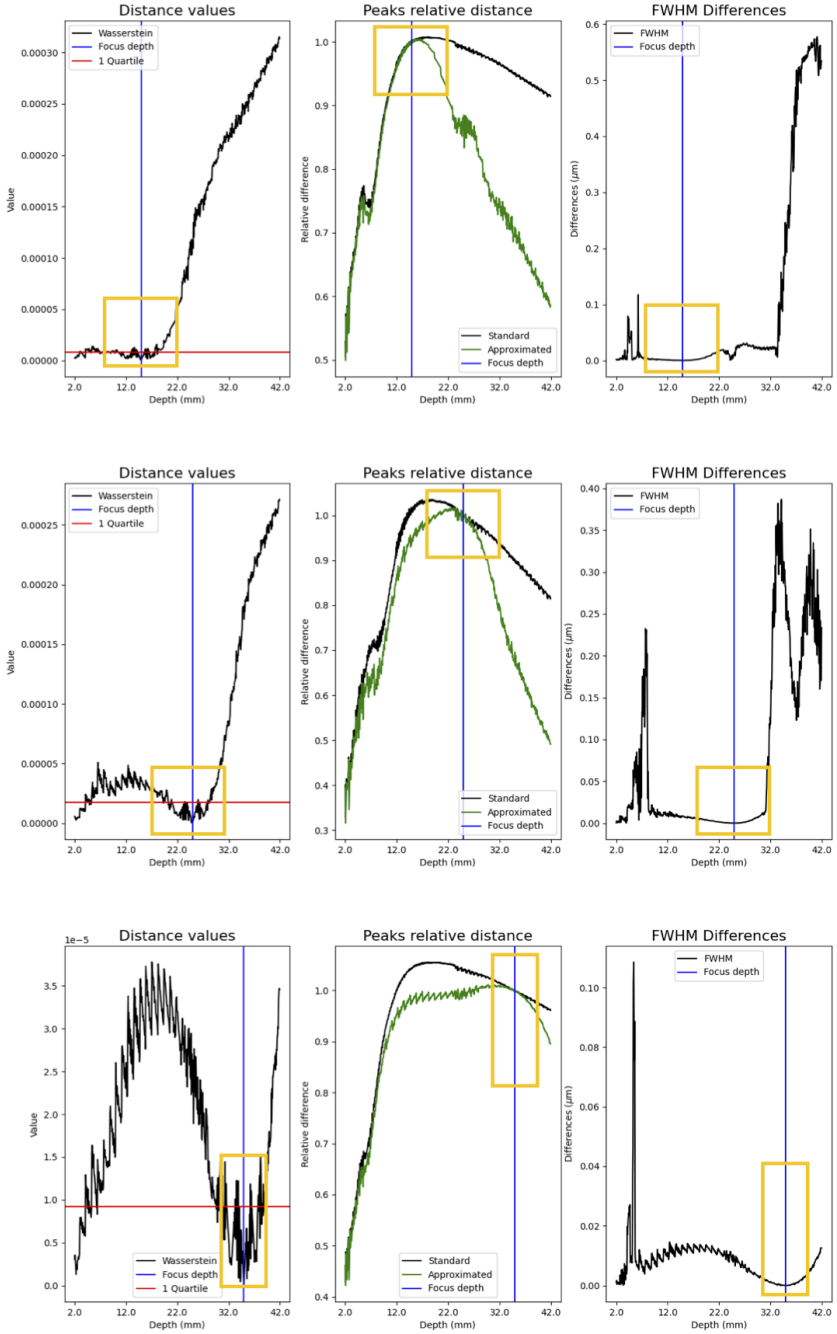

Figure 6.8: Fixing $k_f = 0.8$, each row shows the results for differerent focal points in increasing order. Moreover, to vary the most the differences of solutions, we have chosen a different frequency for each row, $8, 6, 4\,MHz$ respectively. Each of the three plot represents the Wasserstain distance, the peaks absolute difference and the FWHM differences respectively. The yellow box underline a possible neighborhood.

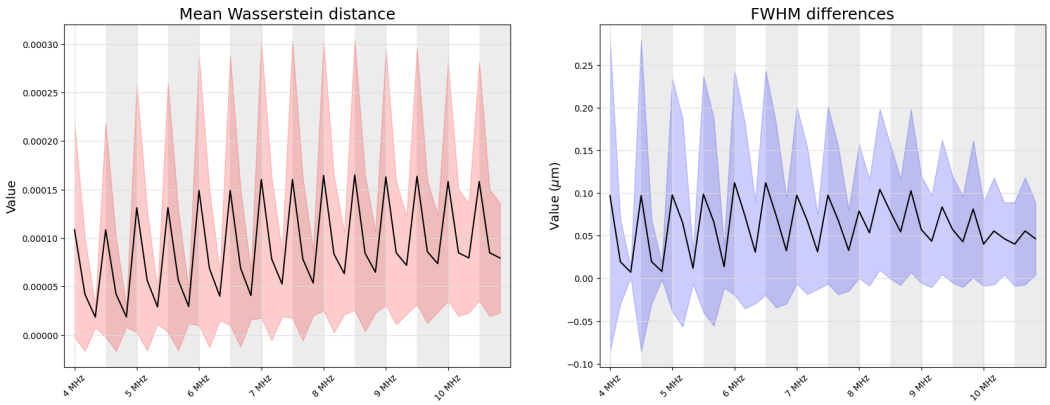

Figure 6.9: Wasserstain distance mean values are displayed on the left side while FWHM differences on the right side. For each choice of frequency (marked on the x axis), k_f (0.6 white background, 0.8 gray blackground) and depth of focus, we compute the mean value over the 600 couple values and display also the standard deviation.

To describe in a concise way the results of several experiments we compute and display some features of the otained reconstructions (see Figure 6.9). Each point of the line represents the mean computed on the values of the Wasserstain distance (on the left side) and of the FWHM differences (on the right side) of the 600 values of each setting. The coloured area identifies the standard variation of the value for each setting. The alternating background identify the experiments with $k_f = 0.6$ in white and with $k_f = 0.8$ in gray. In each zone we have the three focal points.

The fact that we have higher values when the focal point is closer to the probe is reasonable as the delay curves vary faster as the flattening of the delay curve is lower. This could mean that a suitable neighborhood to apply the same delay curve varies in size, becoming bigger with increasing depth of focus.

These results confirm we could find a local time invariant approximation of classical DAS algorithm. Writing a model with a rescaling factor could lead to performing exactly as DAS. In this scenario, the number of convolutions needed to reconstruct a line should downgrade to the number of focal points choosen. In the next paragraph we introduce a way to determine the weights

by starting from the collection of received signals, which are available not only in simulations but in real imaging applications.

6.4 Adaptive model for time-invariant DAS

In this paragraph, we present an approximation of standard DAS algorithm with constant receiving delays by introducing a rescaling factor to the PSF $\hat{\gamma}(\vec{r})$ as discussed in 6.3.

We start defining the approximation according to the experiments by adding a multiplicative weight depending on the scatterer position and using for the reconstruction the delays of the trasmission focal point. We write:

$$\tilde{\gamma}^{\vec{r}} = \theta_{\vec{r}} \sum_{n \in N} S_n^{F,\vec{r}} * \delta_{D_n^F}, \tag{6.11}$$

where $\theta_{\vec{r}} \in \mathbb{R}$ is the multiplicative weight to be determined. We expect $|\theta_{\vec{r}}|$ to be exactly 1 when the scatterer position is in the transmission focus. Our goal is to find the weight $\theta_{\vec{r}}$ such that

$$\tilde{\gamma}^{\vec{r}} \approx \gamma^{\vec{r}}. \tag{6.12}$$

To do so, we compute the norm of the difference between the two reconstruction:

$$\begin{aligned}
\left|\left|\tilde{\gamma}^{\vec{r}} - \gamma^{\vec{r}}\right|\right|_2^2 &= \left|\left|\theta_{\vec{r}} \sum_{n \in N} S_n^{F,\vec{r}} * \delta_{D_n^F} - \sum_{n \in N} S_n^{F,\vec{r}} * \delta_{D_n(z)}\right|\right|_2^2 \\
&= \left|\left|\sum_{n \in N} \left(\theta_{\vec{r}} S_n^{F,\vec{r}} * \delta_{D_n^F} - S_n^{F,\vec{r}} * \delta_{D_n(z)}\right)\right|\right|_2^2 \\
&= \left|\left|\sum_{n \in N} S_n^{F,\vec{r}} * \left(\theta_{\vec{r}} \delta_{D_n^F} - \delta_{D_n(z)}\right)\right|\right|_2^2
\end{aligned}$$

Applying Plancherel theorem, we have the equality with the same equation in

time-frequency domain:

$$\left|\left|\tilde{\gamma}^{\vec{r}} - \gamma^{\vec{r}}\right|\right|_2^2 = \left|\left|\sum_{n\in N} \hat{S}_n^{F,\vec{r}}(f)\left(\theta_{\vec{r}} e^{-i2\pi f D_n^F} - e^{-i2\pi f D_n(z)}\right)\right|\right|_2^2 \tag{6.13}$$

From now on, we denote by:

$$\begin{cases} s_n := \hat{S}_n^{F,\vec{r}}(f) \\ x_n := e^{-i2\pi f D_n^F} \\ y_n := e^{-i2\pi f D_n(z)} \end{cases} \qquad \begin{cases} S := \left(s_{-\overline{N}}, \cdots, s_{-1}, s_0, \cdots, s_{\overline{N}-1}\right) \\ \mathbf{x} := \left(x_{-\overline{N}}, \cdots, x_{-1}, x_0, \cdots, x_{\overline{N}-1}\right) \\ \mathbf{y} := \left(y_{-\overline{N}}, \cdots, y_{-1}, y_0, \cdots, y_{\overline{N}-1}\right) \end{cases}$$

By using the properties of the norm, and considering $f \in [f_m, f_M]$ the finite interval of suitable frequencies (the recorded signal is band limited), we have:

$$\begin{aligned} \left|\left|\tilde{\gamma}^{\vec{r}} - \gamma^{\vec{r}}\right|\right|_2^2 &= \int_{f_m}^{f_M} \left(\sum_{u\in N} s_u\left(\theta_{\vec{r}} x_u - y_u\right)\right)^* \sum_{v\in N} s_v\left(\theta_{\vec{r}} x_v - y_v\right) df \\ &= \int_{f_m}^{f_M} \left(\sum_{u,v\in N} \left(\theta_{\vec{r}} x_u - y_u\right)^* s_u^* s_v\left(\theta_{\vec{r}} x_v - y_v\right)\right) df \\ &= \int_{f_m}^{f_M} \sum_{u,v\in N} \left(\theta_{\vec{r}} x_u - y_u\right)^* s_u^* s_v \left(\theta_{\vec{r}} x_v - y_v\right) df \\ &= \int_{f_m}^{f_M} \sum_{u,v\in N} s_u^* s_v \left(x_u^* \theta_{\vec{r}} - y_u^*\right)\left(\theta_{\vec{r}} x_v - y_v\right) df \\ &= \int_{f_m}^{f_M} \sum_{u,v\in N} s_u^* s_v \left(\theta_{\vec{r}}^2 x_u^* x_v - \theta_{\vec{r}} x_u^* y_v - \theta_{\vec{r}} x_v y_u^* + y_u^* y_v\right) df \end{aligned}$$

We observe that:

$$\left(\sum_{u,v\in N} s_u^* s_v (x_u^* y_v)\right)^* = \sum_{u,v\in N} s_v^* s_u (y_v^* x_u) = \sum_{u,v\in N} (y_u^* x_v) s_u^* s_v. \tag{6.14}$$

Thus, we obtain:

$$\begin{aligned}\left|\left|\tilde{\gamma}^{\vec{r}} - \gamma^{\vec{r}}\right|\right|_2^2 &= \int_{f_m}^{f_M} \sum_{u,v\in N} \theta_{\vec{r}}^2 \left(x_u^* s_u^* s_v x_v\right)\, df + \\ &- 2\theta_{\vec{r}} \int_{f_m}^{f_M} \sum_{u,v\in N} \Re(s_u^* s_v (x_v y_u^*))\, df + \\ &+ \int_{f_m}^{f_M} \sum_{u,v\in N} \left(y_u^* s_u^* s_v y_v\right)\, df \\ &= \theta_{\vec{r}}^2 \left|\left|S\mathbf{x}\right|\right|^2 - 2\theta_{\vec{r}} \int_{f_m}^{f_M} \Re\left(S^* S \mathbf{y}^* \mathbf{x}\right)\, df + \left|\left|S\mathbf{y}\right|\right|^2,\end{aligned}$$

where we exploited the fact the sum is over all the indexes: while S^*S is real, this may not be true for the product $\mathbf{y}^*\mathbf{x}$ but the imaginary terms vanish by computing the sum as they always compare two times each with switched indexes. Thus, by denoting $I := \int_{f_m}^{f_M} \Re\left(S^* S \mathbf{y}^* \mathbf{x}\right)\, df$, it holds:

$$\left|\left|\tilde{\gamma}^{\vec{r}} - \gamma^{\vec{r}}\right|\right|_2^2 = \theta_{\vec{r}}^2 \left|\left|S\mathbf{x}\right|\right|^2 - 2\theta_{\vec{r}} I + \left|\left|S\mathbf{y}\right|\right|^2 \tag{6.15}$$

We define the operator

$$\begin{aligned}\mathcal{L} : \mathbb{R} &\to \mathbb{R} \\ \theta_{\vec{r}} &\mapsto \mathcal{L}(\theta_{\vec{r}})\end{aligned} \tag{6.16}$$

that associates a value of $\theta_{\vec{r}}$ to the second term of equation (6.15) when the other factors are determined by the experiment setting.

6.4.1 Estimation of rescaling factor $\theta_{\vec{r}}$

Now, we find the best $\theta_{\vec{r}}$ that minimizes the difference between $\tilde{\gamma}^{\vec{r}}$ and $\gamma^{\vec{r}}$. We want to solve the following minimum problem:

$$\min_{\theta_{\vec{r}} \in \mathbb{R}} \mathcal{L}(\theta_{\vec{r}}) \tag{6.17}$$

The derivative with respect to $\theta_{\vec{r}}$ is:

$$\frac{d}{d\vec{r}}\mathcal{L} = 2\theta_{\vec{r}} \, ||S\mathbf{x}||^2 - 2I \tag{6.18}$$

and it is equal to zero in:

$$\theta_{\vec{r}} = \frac{I}{||S\mathbf{x}||^2}. \tag{6.19}$$

Indeed, we can rewrite equation (6.15) as paraboloid in the variable $\theta_{\vec{r}}$:

$$\mathcal{L}(\theta_{\vec{r}}) = \left(\theta_{\vec{r}} - \frac{I}{||S\mathbf{x}||^2}\right)^2 + \frac{||S\mathbf{y}||^2}{||S\mathbf{x}||^2} - \frac{I^2}{||S\mathbf{x}||^2} \tag{6.20}$$

Hence, the stationary point found is a minimum. Thereafter, we could try using

$$\theta^*_{\vec{r}} := \frac{I}{||S\mathbf{x}||^2} \tag{6.21}$$

as possible optimum scaling parameter for our approximation. It is worth noticing we have found a scaling parameter dependent from the received signal. This makes our approximation, defined in eq (6.11), adaptive with respect to the signal. Further studies on the estimation of $\theta_{\vec{r}}$ includes the use of weighted norms in the function spaces allowing to correct the shape of $\tilde{\gamma}$ mainly close to the focal point.

6.4.2 Convolutional DAS model

By approximating the term $\delta_{D_n(\vec{r})}$ in the definition of DAS algorithm with the term $\theta_{\vec{r}}\delta_{D_n^F}$, we can define a convolutional method to reconstruct the central

line. This is possible thanks to the definition on $\tilde{\gamma}$ in which the convolution is no longer dependent from the space but is a true convolution. Indeed, this formulation of the algorithm could reduce significantly its computational cost. By choosing a fixed number of focus point along the line in transmission $\vec{F}_1, \cdots, \vec{F}_Q$, and associating them the scaling parameter sets for all the points in their neighbourhood $\Theta_1, \cdots, \Theta_Q$, we have a partition of the line to reconstruct. Thus, the line can be reconstructed performing Q convolutions resulting in the reconstruction of several portions of the signal $\Gamma_1, \cdots, \Gamma_Q$, where:

$$\Gamma_q := \Theta_q \sum_{n \in N} S_n^{F_q} * \delta_{D_n^q} \quad \forall q \in Q \tag{6.22}$$

By collecting the values of each portion we get the entire line:

$$L_{\mathcal{I}} := \left\{ \Gamma_q \right\}_{q \in Q} \tag{6.23}$$

6.5 Preliminary results

We present some prelimirary results obtained by the same settings used in section 6.3. In particular, we have the same 42 different configurations by varying the central frequencies, the Kossoff parameters and the focal depths. For each configuration, we have estimated $\theta_{\vec{r}}$ and reconstructed the 1D PSF according to $\tilde{\gamma}$ formulation in eq. (6.11).

To perform the experiments we have choosen to use

$$\tilde{\theta}_{\vec{r}} := \frac{\max_{t \in \mathbb{R}_+} \gamma(t)}{\max_{t \in \mathbb{R}_+} \tilde{\gamma}(t)}. \tag{6.24}$$

Although it is not the theoretical prescription proposed in section 6.4, it is a reasonable choice for compensating the differences in the peaks heigths described in section 6.3.

We display the values of $\tilde{\theta}_{\vec{r}}$ in each setting in Figure 6.10. Clearly in the transmission focal point $\tilde{\theta}_{\vec{r}}$ is equal to 1. It is reasonable that the values increase

faster when the focal point is closest to the probe than in the other cases as the signal attenuates along depth. To reconstruct the 600 1D PSFs, we have used 1024 time samples, each coresponding to $0.01\mu s$, where t_0 is the first time at which the target point is hit by the transmitted wave. Therefore, the time interval lasts $10.24\mu s$ for each point thus being much longer than the time required to reconstruct the signal dispersion of a single scatterer. This choice leads to have many samples of γ and $\tilde{\gamma}$ negligible with respect to the peaks heights. Indeed, to estimate the error we compute:

$$E_{\%} := \frac{\left|\left|\tilde{\gamma}^{\vec{r}} - \gamma^{\vec{r}}\right|\right|_2}{\left|\left|\gamma^{\vec{r}}\right|\right|_2}. \tag{6.25}$$

In Figure 6.11, we display the obtained results. In each plot we represent, for each couple of transmission central frequency and Kossoff parameter, a possible choice of neighborhood for each focal depth by filling the area in which $E_{\%}$ is less then a certain threshold (5, 7.5, 10 %). We can observe the amplitude of the neighborhoods seems to stabilize at increasing transmission central frequency. By choosing lower thresholds the neighborhoods size decrease, then the convolutional approach proposed in eq. (6.22) needs higher density of focus points along the line. To better evaluate how many focal points we need to reconstruct the line, we can look at Figure 6.12, in which for each experiment we display the number of pixels contained in the coloured areas. It is clear the worst case is achieved when $f_0 = 10\,MHZ$ and the threshold is set to 5%. In this case, the neighborhoods contain about 25 pixels that compared with the 600 composing the line lead to a possible choice of 24 focal points. This means our line could be reconstructed computing 24 convolutions as described in eq. (6.22), compared to the 600 oned used by eq. (6.6).

Although these are preliminary results, we think this is an encouraging result. The next step will include the evaluation of achievable results by estimating the paramenter according to eq. (6.21).

Furtermore, at this point, our method includes many transmission focal point that may reduce the frame rate in real applications. To perform only a

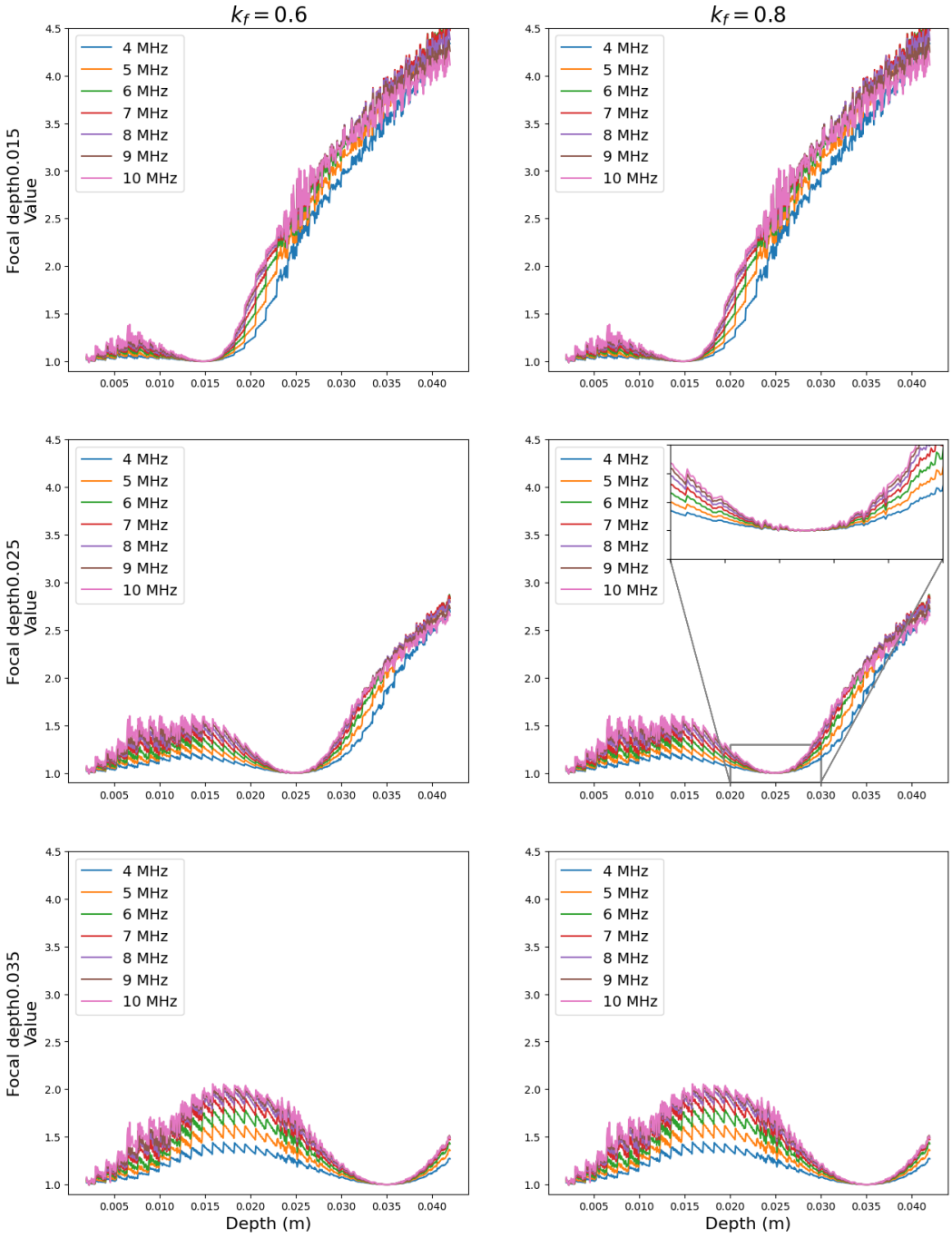

Figure 6.10: Preliminary results of θ estimation. Each row corresponds to a different focal depth in transmission while on the column is k_f to vary. In each plot we display the values for all the seven frequencies.

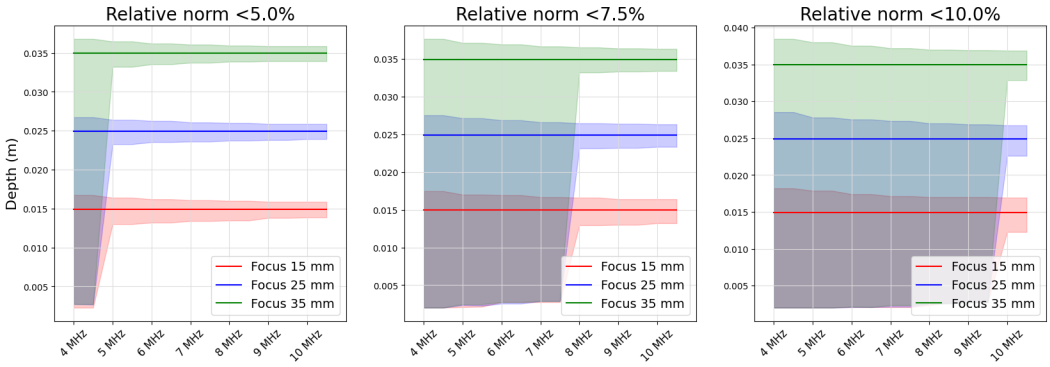

Figure 6.11: In each of three plots we represent the neighborhoods estimated for different tolerance of error. For each frequency we have two different possible values coresponding to the two possibilities od k_f. Each color represents a different focal depth, the coloured area highlights the area in which the relative error is under the tolerance.

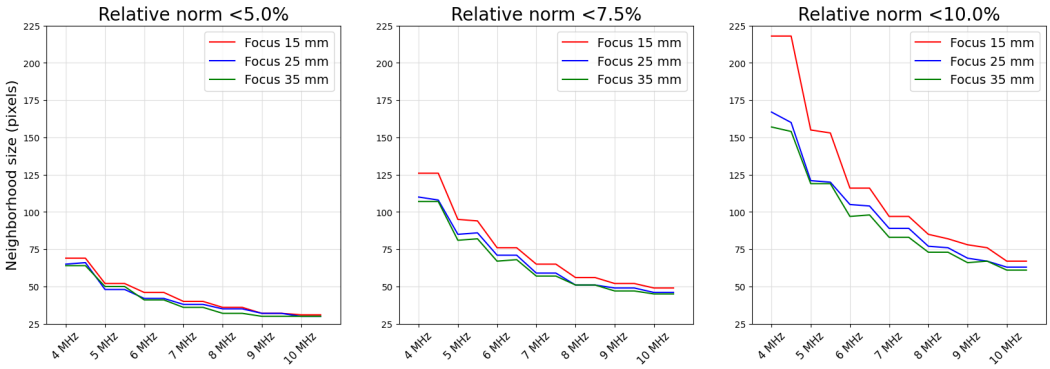

Figure 6.12: In the same settings used in Figure 6.11, we plot the number of pixels reconstructed with relative error under the tolerance corresponding to the coloured area in the previous picture.

transmission to reconstruct the entire line a possible solution may be to chose a focal point and reconstruct the approximations fixing the curve of another point $\vec{R}$ for all the points. To explore this possibility we have to evaluate the exact position of the points that can be chosen and if there is a criterium to relate the position $\vec{F}$ and $\vec{R}$.

We will look further to develop the theoretical model in more detail by including the possibility of applying the scaling parameter specifically only on the most significant times. This may reduce the effects on the background noise in this 1D case.

Therefore, we will explore the 2D case: we need to evaluate the effect our approximation could have on the side lobes generated. We may need to consider all the lateral coordinates to tune finely the scale parameter to affect the least possible the background noise.

Chapter 7

Conclusions

In this thesis we investigate the ultrasound imaging problem by analizing first the signal transmission problem, relevant to some specific applications such as the ARFI and the Doppler technique, and then the reconstruction phase, the usual B-mode imaging method. Both these problems depend on some specific parameters and the main goal of this work was the estimation of such parameters for some particular applications.

We can summarize the main contributions of this work as follows

1. a mathematical framework which uses a hybrid time-frequency domain formulation for modeling beam patterns during the transmission step. This framework defines the parameter space as an N-dimensional torus.

2. The introduction of a novel simulator, parUST [71], designed for generating beam patterns based on this framework. The study includes experimental validation using simulated ultrasound data.

3. An effective approach for optimizing the narrowband transmit beam pattern, thus providing a method that aims to ultimately improve accuracy and reduce artifacts in important medical ultrasound applications with a particular focus on ARFI elastography imaging.

4. An adaptive model for time-invariant DASin order to develop an alternative fast convolutional algorithm for B-mode image reconstruction.

As far as the transmission phase is concerned, the developed model possesses several advantageous features. Firstly, it adopts a two-step approach that enables the pre-computation of the system frequency response for a given probe model and region of interest. This methodology proves particularly effective when the simulator is employed as a kernel in optimization problems, whether gradient-based or non-gradient-based, requiring testing of numerous transmit parameter sets for beam pattern shape. In contrast, the reference simulator, FIELD II, has a monolithic structure that needs restarting all computations each time a single parameter is altered. Secondly, our frequency domain approach eliminates time oversampling, simplifying time convolutions between impulse responses and waveform or attenuation terms to element-wise products on a limited set of frequency bins. Additionally, it specializes in the narrowband case with a single frequency computation, resulting in significant computational savings compared to FIELD II-like time-domain approaches. This narrowband case formulation also facilitates the investigation of space transmit delays' topology, paving the way to suitable manifold optimization.

The simulator is an open-source Python package optimized with parallel computations, providing a high-performance, trusted tool for parameter optimization processes on manifolds for beam pattern formation. Numerical tests demonstrate that the proposed model is both computationally efficient and compatible with realistic measurements and existing numerical simulators, contributing to the design of new medical diagnostic ultrasound equipment.

Taking advantage of this numerical model, we devised an optimization scheme to deal with transmission delays optimization. The method yields sets of beam patterns that exhibit uniformity along depth in terms of both BP width and intensity, with low side lobe levels, meeting the desired requirements for typical biomedical ultrasound applications. Moreover, the application to ARFI elastography yields comparable results in terms of shear wave peak intensity and even better results in terms of standard deviation of time of flights and velocity estimation. We emphasize that, while we do not specifically address

imaging improvements, our method provides quantitative tools to assess the strengths of our optimization approach.

The adopted strategy facilitates extending calculations to convex probes through a simple change from Cartesian to polar coordinates, as well as to steered beam patterns. Despite these strengths, our work has limitations. The advantages of the method are not demonstrated with optimized BPs having different numbers of active elements or with different BP shapes. A potential expansion could involve experimenting with neural networks using various ground truth shapes as inputs and optimized delays as outputs. Future developments will also include apodization weights in the set of optimized variables, compensating for the slight deterioration of side lobe level observed with the present method compared to standard delay laws [82].

Taking advantage of this numerical model, by starting from some considerations of the geometry on the dynamic focusing problem, we developed a very simple approximate model for DAS. The strength of this model lies in the fact that, by drastically lowering the computational cost due to its pure convolutional form, it could be a faster approximation of the DAS algorithm. Although the study is currently confined to a specific 1D case, we hope to develop the model to reconstruct an entire line with one, or at least few, transmissions. Further development of our theoretical model involves considering the scaling parameter application specifically during significant times to reduce background noise in the 1D case. Additionally, we plan to explore the 2D scenario to assess the effect of our approximation on generated side lobes. Tuning the scale parameter across all lateral coordinates may minimize background noise effects.

Appendix A

Principal Component Analysis

The primary purpose of principal component analysis is to obtain a graphical representation of the joint distribution of p numerical variables when $p > 2$. Through this technique, it is also possible to visualize the correlation between variables. The goal is to identify low dimensional representations of the point that maintain the greatest dispersion of points, thus ensuring better identification [26, 44, 68].

The reduction in the dimensionality of the space is performed replacing the original p variables with a new set of q variables (called principal components), which are linear combinations of the original ones.

The basic idea is to perform a translation of the axes by aligning the new origin with the centroid of the data. Subsequently, new axes are sought such that the variance of the projections of the points onto the first new axis is maximized, the variance onto the second new axis is maximized once the first axis is fixed, and so on. In detail, the system of axes that satisfies the preceding conditions is the one formed by the eigenvectors (ordered decreasingly) associated with the eigenvalues of the correlation (or covariance) matrix of the variables.

We denote by X the $n \times p$ matrix containing the $X_1, \cdots, X_p$ feature columns for n experiments and by $\Gamma(X)$ its correlation matrix. If we denote by Y the

matrix containing the standardized variables, it holds

$$\Gamma(X) = \frac{1}{n} Y^t Y.$$

The rank of $\Gamma(X)$ is equal to the rank of Y, that is, the range of X; it can be initially assumed that the p statistical observations are linearly independent, and therefore the rank of $\Gamma(X)$ is p (otherwise, non-independent variables are not considered). It is also assumed that there are no multiple eigenvalues. Additionally, if the row points of Y are orthogonally projected along the direction of a vector, the distances from the origin of the obtained points can be considered as values of a new variable. This new variable is a linear combination of the variables $Y_1, Y_2, ..., Y_p$.

As previously mentioned, to find a reduced-dimensional space in which to project the data while losing the least amount of information possible, a suitable change of coordinates is performed. This is done so that the projections of the points with respect to the first coordinate axes are the flat representations that maintain the maximum dispersion of the data.

The new axes originate from the centroid of the data (whether considering the correlation matrix or the covariance matrix). Furthermore, the direction of the first axis coincides with the greatest intensity of point dispersion, and the direction of the second axis (which must be orthogonal to the first) coincides with the greater dispersion of all subsequent axes, and so on.

The dispersion of the projected points is measured by the variance of the variable containing the distances from the origin of the projected points. The orthonormal basis that has the desired characteristics consists of the eigenvectors of the matrix $\Gamma(X)$ associated with the eigenvalues arranged in decreasing order.

Proposition 1. *Let $(u_1, \cdots, u_p)$ be the eigenvectors of the matrix $\Gamma(X)$ associated with the eigenvalues $\lambda_1, \cdots, \lambda_p$, ordered in decreasing order. Let C_j be the vector with the new $j-th$ coordinates of the n points of Y:*

$$C_j = Y u_j.$$

The following results hold:

1. *the mean and variance of the points projected along the $j-th$ vector u_j are, respectively:*

$$\mathbb{E}(C_j) = 0 \quad \mathbb{V}(C_j) = \lambda_j$$

2. *The vectors of the projections of the points onto $(u_1, \cdots, u_p)$ are pairwise uncorrelated.*

$$\text{cov}(C_i, C_j) = 0 \quad \textit{if} \quad i \neq j$$

3. *If v is a vector of length 1 in $\mathbb{R}^p$, then:*

   - *the variance of the points projected along u_1 is the largest among the variances of the points projected along any generic unit vector in $\mathbb{R}^p$:*

$$\mathbb{V}(C_1) = \sup_{v \in \mathbb{R}^p} \{\mathbb{V}(Yv)\, s.t.\, ||v|| = 1\}$$

   - *The variance of the points projected along u_j is the largest among the variances of the points projected along any generic vector uncorrelated with $C_1, \cdots, C_{j-1}$:*

$$\mathbb{V}(C_j) = \sup_{v \in \mathbb{R}^p} \left\{\mathbb{V}(Yv) s.t. ||v|| = 1, Yv \textit{ uncorrelated with } C_1, \cdots, C_{j-1}\right\}$$

Proof. If we denote by $(e_1, \cdots, e_p)$ the canonical base for $\mathbb{R}^p$, it holds:

1.

$$\bar{C}_j = \overline{Yu_j} = 0 \tag{A.1}$$

$$\mathbb{V}\left(C_j\right) = \mathbb{V}\left(Yu_j\right) = u_j^t \Gamma u_j = u_j^t U \Lambda U^t u_j = e_j^t \Lambda e_j = \lambda_j \tag{A.2}$$

2. $\text{cov}\left(C_i, C_j\right) = \text{cov}\left(Yu_i, Yu_j\right) = u_i^t U \Lambda U^t u_j = e_i^t \Lambda e_j = 0$, if $i \neq j$

3. if $v \in \mathbb{R}^p$ and $v^t v = 1$, then:

$$\mathbb{V}(Yv) = v^t U \Lambda U^t v = \left(U^t v\right)^t \Lambda \left(U^t v\right) = \tilde{v}^t \Lambda \tilde{v} = \left(\Lambda^{1/2} \tilde{v}\right)^t \left(\Lambda^{1/2} \tilde{v}\right)$$

where $\tilde{v}$ is vector v in the new basis, then is length is still 1. Thus, $\mathbb{V}(Yv) = \left(\Lambda^{1/2}\tilde{v}\right)^t \left(\Lambda^{1/2}\tilde{v}\right) = \sum_{j=1}^{p} \tilde{v}_j^2 \lambda_j \leq \lambda_1 \sum_{j=1}^{p} \tilde{v}_j^2 = \lambda_1 = \mathbb{V}(C_1)$. The equality holds if $\tilde{v} = u_1$. The second statement follows using the Langrange's multiplier method.

□

The eigenvector u_j is called the $j-th$ principal axis of the data. The vector C_j is called the $j-th$ principal component and is uniquely determined up to sign (if λ_j is a simple eigenvalue, i.e., of multiplicity 1, which is almost always the case in the context of statistical observations). The elements of the principal axes are referred to as principal loadings, whereas the elements of the linear combination generating the principal components are referred to as scores.

The principal components C_j can be interpreted as new variables, being linear combinations of the original variables.

As previously observed, the principal components $C_1, \cdots, C_p$ have the following properties:

1. They have mean 0.
2. They have variances $\lambda_1, \ldots, \lambda_p$ in decreasing order, i.e., $\lambda_1 \geq \ldots \geq \lambda_p$.
3. They are pairwise uncorrelated.

It's important to note that the principal components are defined up to sign; the orientation of the axes is arbitrary and depends on the algorithm used to construct the matrices Λ and U.

A.1 Relationship between PCA and Singular Value Decomposition (SVD)

We denote by $\tilde{(X)}$ the centered values data matrix corresponding to X.

It holds that the associated covariance matrix C can be obtained as:

$$C = \frac{\tilde{X}^t \tilde{X}}{n-1}. \tag{A.3}$$

As C is symmetric, it can be diagonalized:

$$C = VLV^t,$$

where L is a diagonal matrix with eigenvalues λ_i in decreasing order on the diagonal and V the corresponding eigenvectors matrix. We apply SVD to matrix $\tilde{X}$, obtaining the following decomposition:

$$\tilde{X} = USV^t,$$

where S is the diagonal matrix of singular values s_i, U is a unitary matrix and V is the right singular vexctor matrix. By substituting the decomposition in eq. (A.3), it holds:

$$C = \frac{VSU^tUSV^t}{n-1} = V\frac{S^2}{n-1}V^t.$$

Thus the right singular vectors V are the principal axis and the principal components are given by $XV = US$.

From the properties of SVD decomposition, it holds that the scatterplot associated to $\tilde{X}$ of rank $r \leq \min n, p$ represent n points in a r-dimensional subspasce of $\mathbb{R}^p$ centered in the centroid of the scatterplot. If we desire to approximate this scatterplot in a q-dimensional subspace, the 'best' subspace is the one in which is minimized the sum of squared distances between corresponding points in each scatterplot [44, 68].

Appendix B

Particle Swarm Optimization

The Particle Swarm Optimization (PSO) algorithm, conceived by Dr. James Kennedy and Dr. Russell Eberhart in 1995 [45], stands out as a potent and adaptable optimization technique inspired by the collective behavior seen in birds and fish. This metaheuristic algorithm can be categorized as a Swarm Intelligence (SI) technique: this class of algorithms defines a system in which agents engage in local interactions with their environment, leading to collective behaviors that give rise to cohesive global patterns. In contrast to Evolutionary Algorithms (EAs), SI techniques draw inspiration from the straightforward behaviors and self-organizing interactions of agents, exemplified by phenomena like fish schooling, honey bee activities, bacterial growth, animal herding, bird flocking, ant colonies foraging, and similar instances [23].

PSO has garnered widespread acclaim due to its simplicity, efficiency, and broad applicability across various optimization problems in different fields such as engineering design, machine learning, and image processing. In the years researchers have extended and customized the PSO algorithm to address a myriad of problem domains, underscoring its adaptability and efficacy in tackling intricate, multidimensional optimization challenges [57, 95, 97, 98].

The swarm in PSO is a collection of potential solutions representing a bird flying with a certain velocity across the solutions space. The movement of each particle is shaped by its individual experience and the shared knowledge within

the swarm. Through a process of iterative refinement, particles dynamically adjust their positions in the search space, progressively converging towards optimal solutions. The algorithm's behavior hinges on two key components: personal best and global best. The personal best denotes the most favorable solution a particle has encountered thus far, while the global best represents the optimal solution discovered by any particle in the entire swarm. These components dictate the trajectory of each particle, fostering exploration of the solution space while exploiting promising areas.

Even if PSO offers the distinct advantage of requiring few parameters to tune, it achieves optimal solutions through interactions among particles, yet when navigating high-dimensional search spaces, it tends to converge at a notably slow pace toward the global optimum. Furthermore, when confronted with complex and expansive datasets, PSO tends to yield sub optimal results. Particularly in scenarios with a substantial number of dimensions, PSO often struggles to uncover the global optimum solution. This challenge arises not solely due to the presence of local optima traps but also because of potential fluctuations in particle velocities [85], restricting the successive range of trials to a sub-plane within the overall search hyperplane.

B.1 PSO structure

The algorithm proceeds, ad a SI system, following the self-organization rules as interpreted by [4]:

- Robust dynamical non linearity: characterized by a combination of positive and negative feedback loops, facilitates the creation of advantageous structures. Positive feedback plays a promotional role in their formation, while negative feedback ensures a counterbalance, contributing to the stabilization of the overall pattern.

- Trade-off between exploration and exploitation: a valuable avenue for fostering creativity in artificial systems lies in the skillful management

of the trade-off between exploration and exploitation. This optimal balance, as identified by SI, offers a means to promote creativity without compromising efficiency.

- Multiple interactions: within a swarm context, multiple interactions occur as individual agents leverage information from neighboring agents. This dynamic allows for the dissemination of information throughout the network, enhancing the collective intelligence of the swarm.

We denote by f the objective function to be optimized, by $\boldsymbol{x}$ the swarm containing N particles. At each iteration t, each particle is characterized by its position $\boldsymbol{x}_i^t$ ant its velocity $\boldsymbol{v}_i^t$. Moreover, we associate a personal best position to each particle $\boldsymbol{p}_{best_i}^t$ and a global best position in the swarm $\boldsymbol{g}_{best_i}^t$, defined as follows:

$$\boldsymbol{p}_{best_i}^t := \min_{k=1,\cdots,t} \left(\left\{ f(\boldsymbol{x}_i^k) \right\} \right) \tag{B.1}$$

$$\boldsymbol{g}_{best_i}^t := \min_{\substack{k=1,\cdots,t \\ i=1,\cdots,N}} \left(\left\{ f(\boldsymbol{x}_i^k) \right\} \right) \tag{B.2}$$

To the swarm we associate three parameters: ω the inertia weight, c_1 the cognitive coefficient, that modules the importance of the personal best result, and c_2 the social coefficient, that modules the importance of the global best solution. Then, if the solution dimension is D, given $\boldsymbol{r}_2$ and $\boldsymbol{r}_2$ random vectors uniformly distributed in $[0,1]^D$, each particle is updated following:

$$\boldsymbol{v}_i^{t+1} = \omega \boldsymbol{v}_i^t + c_1 \boldsymbol{r}_1 \left(\boldsymbol{p}_{best_i}^t - \boldsymbol{x}_i^t \right) + c_2 \boldsymbol{r}_2 \left(\boldsymbol{g}_{best}^t - \boldsymbol{x}_i^t \right) \tag{B.3}$$

$$\boldsymbol{x}_i^{t+1} = \boldsymbol{x}_i^t + \boldsymbol{v}_i^t. \tag{B.4}$$

Referring to the velocity update in (B.3), the inertia component (first part) embodies the preceding velocity. This component imparts suitable momentum to the particles, enabling them to traverse the search space. The cognitive component signifies the individual positivity for each particle, the term make

them progress towards their best-known positions from prior iterations. Finally, the third segment, "social component," reflects the combined influence of all particles, working collaboratively to attain the global optimum solution.

We report a pseudocode for PSO in the case of a minimization task:

Algorithm 2 PSO algorithm

Require:
Initialize randomly $\boldsymbol{v}^0$ and $\boldsymbol{x}^0$
Set $\boldsymbol{p}^0_{best_i} = \boldsymbol{x}^0 \quad \forall\, i\ in 1, \cdots, N$
Find $\boldsymbol{g}^0_{best}$ according to Eq. (B.2)
Set $t = 1$
while $t \leq T$ **do**
  for $i = 1$ to N **do**
    Generate $\boldsymbol{r}_2$ and $\boldsymbol{r}_2$ random
    Update velocity according to Eq. (B.3)
    Update position according to Eq. (B.4)
    if $f(\boldsymbol{x}^t_i) > f(\boldsymbol{p}^{t-1}_{best_i})$ **then**
      $f(\boldsymbol{p}^t_{best_i}) = f(\boldsymbol{x}^t_i)$
    end if
  end for
  Update global best position $\boldsymbol{g}^t_{best}$ according to Eq. (B.2)
  t = t+1
end while

Bibliography

[1] "A new calculation procedure for spatial impulse responses in ultrasound". In: *The Journal of the Acoustical Society of America* 105.6 (June 1999), pp. 3266–3274. ISSN: 0001-4966. DOI: 10.1121/1.424654. eprint: https://pubs.aip.org/asa/jasa/article-pdf/105/6/3266/8086297/3266_1_online.pdf. URL: https://doi.org/10.1121/1.424654.

[2] P.-A. Absil, R. Mahony, and R. Sepulchre. *Optimization Algorithms on Matrix Manifolds*. Princeton: Princeton University Press, 2008. ISBN: 9781400830244. DOI: doi:10.1515/9781400830244. URL: https://doi.org/10.1515/9781400830244.

[3] A. Besson, J. Thiran, and Y. Wiaux. "Imaging from Echoes: On Inverse Problems in Ultrasound". PhD thesis. Ecole Polytechnique Fédérale de Lausanne, 2019.

[4] Eric Bonabeau, Marco Dorigo, and Guy Theraulaz. *Swarm Intelligence: From Natural to Artificial Systems*. Oxford University Press, Oct. 1999. DOI: 10.1093/oso/9780195131581.001.0001.

[5] Silvère Bonnabel. "Stochastic Gradient Descent on Riemannian Manifolds". In: *IEEE Transactions on Automatic Control* 58.9 (2013), pp. 2217–2229. DOI: 10.1109/TAC.2013.2254619.

[6] N. Boumal. *An introduction to optimization on smooth manifolds*. Cambridge University Press, 2023. DOI: 10.1017/9781009166164. URL: https://www.nicolasboumal.net/book.

[7] T. Bruyneel et al. "A GPU-based implementation of the spatial impulse response method for fast calculation of linear sound fields and pulse-echo responses of array transducers". In: *2013 IEEE International Ultrasonics Symposium (IUS)*. 2013, pp. 367–369. DOI: 10.1109/ULTSYM.2013.0095.

[8] Giovanni Cardone et al. "Optimization of wide-band linear arrays". In: *IEEE transactions on ultrasonics, ferroelectrics, and frequency control* 48.4 (2001), pp. 943–952.

[9] Z. Chen, A. Basarab, and D. Kouamé. "Compressive deconvolution in medical ultrasound imaging". In: *IEEE Transactions on Medical Imaging* 35.3 (2016), pp. 728–737. DOI: 10.1109/TIP.2007.910179.

[10] T. Chernyakova and Y. C. Eldar. "Fourier-domain beamforming: the path to compressed ultrasound imaging". In: *IEEE Transactions on Ultrasonics, Ferroelectrics, and Frequency Control* 61.8 (2014), pp. 1252–1267. DOI: 10.1109/TUFFC.2014.3032.

[11] R. S. C. Cobbold. *Foundations of Biomedical Ultrasound*. Biomedical engineering series. Oxford University Press, 2007. ISBN: 9780195168310. URL: https://books.google.it/books?id=NVJRAAAAMAAJ.

[12] P. Crombie, A. Bascom, and S. Cobbold. "Calculating the pulsed response of linear arrays: Accuracy vs. computational efficiency". In: *IEEE Trans. Ultrason. Ferroelect. Freq. Contr.* 44 (1997), pp. 997–1009.

[13] C. Cueto et al. "Stride: A flexible software platform for high-performance ultrasound computed tomography". In: *Computer Methods and Programs in Biomedicine* 221 (2022), p. 106855. DOI: https://doi.org/10.1016/j.cmpb.2022.106855. URL: https://www.sciencedirect.com/science/article/pii/S0169260722002371.

[14] Jacques Curie and Pierre Curie. "Développement par compression de l'électricité polaire dans les cristaux hémièdres à faces inclinées". In: 1880.

[15] Simone Curletto, Maria Palmese, and Andrea Trucco. "On the optimization of the transmitted beam in contrast-enhanced ultrasound medical imaging". In: *IEEE Transactions on Instrumentation and Measurement* 56.4 (2007), pp. 1239–1248.

[16] Simone Curletto and A Trucco. "Main lobe shaping in wide-band arrays". In: *Oceans 2003. Celebrating the Past... Teaming Toward the Future (IEEE Cat. No. 03CH37492)*. Vol. 5. IEEE. 2003, SP2869–SP2874.

[17] Thomas Deffieux et al. "The variance of quantitative estimates in shear wave imaging: theory and experiments". In: *IEEE transactions on ultrasonics, ferroelectrics, and frequency control* 59.11 (2012), pp. 2390–2410.

[18] Joshua R Doherty, Jeremy J Dahl, and Gregg E Trahey. "Harmonic tracking of acoustic radiation force-induced displacements". In: *IEEE transactions on ultrasonics, ferroelectrics, and frequency control* 60.11 (2013), pp. 2347–2358.

[19] I Donald. "Mac, vicar J, Brown TG (1958) Investigation of abdominal masses by pulsed ultrasound". In: *Lancet I* 1188 (1958).

[20] K T Dussik, F Dussik, and L Wyt. "Towards hyperphonography of the brain". In: *Wien. Med. Wochenschr.* 97.38-39 (1947), pp. 425–429.

[21] I Edler. "The use of ultrasonic reflectoscope for the continuous recording of the movements of heart walls". In: *Kungl Fysiogr sallsk i Lund forhandl* 24 (1954), pp. 1–19.

[22] F. Stuart Foster and J. W. Hunt. "Transmission of ultrasound beams through human tissue—focussing and attenuation studies". In: *Ultrasound in Medicine & Biology* 5.3 (1979), pp. 257–268. ISSN: 0301-5629. DOI: https://doi.org/10.1016/0301-5629(79)90017-6. URL: https://www.sciencedirect.com/science/article/pii/0301562979900176.

[23] A.G. Gad. "Correction to: Particle Swarm Optimization Algorithm and Its Applications: A Systematic Review". In: *Arch Computat Methods* (2022). DOI: 10.1007/s11831-022-09762-3.

[24] D. Garcia. "SIMUS: An open-source simulator for medical ultrasound imaging. Part I: Theory & examples". In: *Computer Methods and Programs in Biomedicine* 218 (2022), p. 106726. ISSN: 0169-2607. DOI: https://doi.org/10.1016/j.cmpb.2022.106726. URL: https://www.sciencedirect.com/science/article/pii/S0169260722001122.

[25] David E. Goldberg. "Genetic Algorithms in Search Optimization and Machine Learning". In: 1988. URL: https://api.semanticscholar.org/CorpusID:38613589.

[26] Michael Greenacre et al. "Principal component analysis". In: *Nature Reviews Methods Primers* 2.1 (2022), p. 100. DOI: 10.1038/s43586-022-00184-w. URL: https://doi.org/10.1038/s43586-022-00184-w.

[27] James F. Greenleaf, Mostafa Fatemi, and Michael Insana. "Selected Methods for Imaging Elastic Properties of Biological Tissues". In: *Annual Review of Biomedical Engineering* 5.1 (2003). PMID: 12704084, pp. 57–78. DOI: 10.1146/annurev.bioeng.5.040202.121623. URL: https://doi.org/10.1146/annurev.bioeng.5.040202.121623.

[28] James F. Greenleaf and Chandra M. Sehgal. "Biologic System Evaluation with Ultrasound". In: *Springer: New York*. 1992. URL: https://api.semanticscholar.org/CorpusID:33153362.

[29] Hao Guo et al. "Fourier-Domain Beamforming and Sub-Nyquist Sampling for Coherent Pixel-Based Ultrasound Imaging". In: *2022 IEEE International Ultrasonics Symposium (IUS)*. 2022, pp. 1–4. DOI: 10.1109/IUS54386.2022.9958356.

[30] G. R. Harris. "Transient field of a baffled planar piston having an arbitrary vibration amplitude distribution". In: *The Journal of the Acoustical Society of America* 70.1 (1981), pp. 186–204.

[31] Yashuo He et al. "Piezoelectric Micromachined Ultrasound Transducer Technology: Recent Advances and Applications." eng. In: *Biosensors (Basel)* 13.1 (Dec. 2022). ISSN: 2079-6374 (Electronic); 2079-6374 (Linking). DOI: 10.3390/bios13010055.

[32] Zhengyao He et al. "A sidelobe suppressing near-field beamforming approach for ultrasound array imaging". In: *The Journal of the Acoustical Society of America* 137.5 (2015), pp. 2785–2790.

[33] Peter Hollender, Nick Bottenus, and Gregg Trahey. "A multiresolution approach to shear wave image reconstruction". In: *IEEE transactions on ultrasonics, ferroelectrics, and frequency control* 62.8 (2015), pp. 1429–1439.

[34] P. Hoskins, K. Martin, and A. Thrush. *Diagnostic Ultrasound: Physics and Equipment*. 2nd ed. Cambridge University Press, 2010. DOI: 10.1017/CBO9780511750885.

[35] Sheng-Wen Huang et al. "Exact viscoelastic Green's functions of the Voigt-model-based Navier's equation". In: *2013 IEEE International Ultrasonics Symposium (IUS)*. 2013, pp. 352–355. DOI: 10.1109/ULTSYM.2013.0091.

[36] E.E. Hundt and E.A. Trautenberg. "Digital Processing of Ultrasonic Data by Deconvolution". In: *IEEE Transactions on Sonics and Ultrasonics* 27.5 (1980), pp. 249–252. DOI: 10.1109/T-SU.1980.31185.

[37] D. Hyun et al. "Beamforming and Speckle Reduction Using Neural Networks". In: *IEEE Transactions on Ultrasonics, Ferroelectrics, and Frequency Control* 66.5 (2019), pp. 898–910. DOI: 10.1109/TUFFC.2019.2903795.

[38] J. A. Jensen. "A model for the propagation and scattering of ultrasound in tissue". In: *J Acoust Soc Am. 1991 Jan* 89 (1991), pp. 182–191. DOI: doi:10.1121/1.400497.

[39] J. A. Jensen. "A multi-threaded version of Field II". In: *2014 IEEE International Ultrasonics Symposium*. 2014, pp. 2229–2232. DOI: 10.1109/ULTSYM.2014.0555.

[40] J. A. Jensen. "FIELD: A program for simulating ultrasound systems". In: *Medical and Biological Engineering and Computing* 34 (Jan. 1996), pp. 351–352.

[41] J. A. Jensen. *Linear description of ultrasound imaging systems: Notes for the International Summer School on Advanced Ultrasound Imaging at the Technical University of Denmark*. English. Technical University of Denmark, Department of Electrical Engineering, 1999.

[42] J. A. Jensen. "Ultrasound Imaging and Its Modeling". In: *Imaging of Complex Media with Acoustic and Seismic Waves*. Berlin, Heidelberg: Springer Berlin Heidelberg, 2002, pp. 135–166.

[43] Mok-Kun Jeong. "A Fourier transform-based sidelobe reduction method in ultrasound imaging". In: *IEEE transactions on ultrasonics, ferroelectrics, and frequency control* 47.3 (2000), pp. 759–763.

[44] Ian T. Jolliffe and Jorge Cadima. "Principal component analysis: a review and recent developments". In: *Philosophical Transactions of the Royal Society A: Mathematical, Physical and Engineering Sciences* 374.2065 (2016), p. 20150202. DOI: 10.1098/rsta.2015.0202. eprint: https://royalsocietypublishing.org/doi/pdf/10.1098/rsta.2015.0202. URL: https://royalsocietypublishing.org/doi/abs/10.1098/rsta.2015.0202.

[45] James Kennedy and Russell Eberhart. "Particle swarm optimization". In: *Proceedings of ICNN'95-international conference on neural networks*. Vol. 4. IEEE. 1995, pp. 1942–1948.

[46] Piotr Kijanka et al. "Robust phase velocity dispersion estimation of viscoelastic materials used for medical applications based on the multiple signal classification method". In: *IEEE transactions on ultrasonics, ferroelectrics, and frequency control* 65.3 (2018), pp. 423–439.

[47] Gordon S. Kino. "Acoustic waves : devices, imaging, and analog signal processing". In: 1987. URL: https://api.semanticscholar.org/CorpusID:135864994.

[48] S. Kirkpatrick, C. D. Gelatt, and M. P. Vecchi. "Optimization by Simulated Annealing". In: *Science* 220.4598 (1983), pp. 671–680. DOI: 10.1126/science.220.4598.671. eprint: https://www.science.org/doi/pdf/

10.1126/science.220.4598.671. URL: https://www.science.org/doi/abs/10.1126/science.220.4598.671.

[49] G. Kossoff. "Analysis of focusing action of spherically curved transducers". In: *Ultrasound in Medicine & Biology* 5.4 (1979), pp. 359–365. ISSN: 0301-5629. DOI: https://doi.org/10.1016/0301-5629(79)90006-1. URL: https://www.sciencedirect.com/science/article/pii/0301562979900061.

[50] William A Kuperman et al. "Optimal time-domain beamforming with simulated annealing including application of apriori information". In: *The Journal of the Acoustical Society of America* 88.4 (1990), pp. 1802–1810.

[51] G.K. Lewis. "Chirped PVDF Transducers for Medical Ultrasound Imaging". In: *IEEE 1987 Ultrasonics Symposium*. 1987, pp. 879–884. DOI: 10.1109/ULTSYM.1987.199085.

[52] Yadong Li and J.A. Zagzebski. "A frequency domain model for generating B-mode images with array transducers". In: *IEEE Transactions on Ultrasonics, Ferroelectrics, and Frequency Control* 46.3 (1999), pp. 690–699. DOI: 10.1109/58.764855.

[53] Jian-Yu Lu, Hehong Zou, and James F. Greenleaf. "Biomedical ultrasound beam forming". In: *Ultrasound in Medicine & Biology* 20.5 (1994), pp. 403–428. ISSN: 0301-5629. DOI: https://doi.org/10.1016/0301-5629(94)90097-3. URL: https://www.sciencedirect.com/science/article/pii/0301562994900973.

[54] A. C. Luchies and B. C. Byram. "Deep Neural Networks for Ultrasound Beamforming". In: *IEEE Transactions on Medical Imaging* 37.9 (2018), pp. 2010–2021. DOI: 10.1109/TMI.2018.2809641.

[55] Paolo Mattesini et al. "Comparative Assessment of Plane Wave Imaging with 256-element CMUT and Single Crystal Probes". In: *2021 IEEE International Ultrasonics Symposium (IUS)*. 2021, pp. 1–3. DOI: 10.1109/IUS52206.2021.9593805.

[56] R. E. McKeighen and M. P. Buchin. "New Techniques for Dynamically Variable Electronic Delays for Real Time Ultrasonic Imaging". In: *1977 Ultrasonics Symposium*. 1977, pp. 250–254. DOI: 10.1109/ULTSYM.1977.196834.

[57] Schneider G. Meissner M Schmuker M. "Optimized Particle Swarm Optimization (OPSO) and its application to artificial neural network training". In: *BMC Bioinformatics* (2006). DOI: 10.1186/1471-2105-7-125.

[58] O. Michailovich and A. Tannenbaum. "Blind Deconvolution of Medical Ultrasound Images: A Parametric Inverse Filtering Approach". In: *IEEE Transactions on Image Processing* 16.12 (2007), pp. 3005–3019. DOI: 10.1109/TIP.2007.910179.

[59] D.M. Mills. "Medical imaging with capacitive micromachined ultrasound transducer (cMUT) arrays". In: *IEEE Ultrasonics Symposium, 2004*. Vol. 1. 2004, 384–390 Vol.1. DOI: 10.1109/ULTSYM.2004.1417744.

[60] P.M.C. Morse and K.U. Ingard. *Theoretical Acoustics*. International series in pure and applied physics. Princeton University Press, 1986. ISBN: 9780691024011. URL: https://books.google.it/books?id=KIL4MV9IE5kC.

[61] Haleh Nazemi et al. "Mass Sensors Based on Capacitive and Piezoelectric Micromachined Ultrasonic Transducers—CMUT and PMUT". In: *Sensors* 20.7 (2020). ISSN: 1424-8220. DOI: 10.3390/s20072010. URL: https://www.mdpi.com/1424-8220/20/7/2010.

[62] Kathy Nightingale. "Acoustic Radiation Force Impulse (ARFI) Imaging: A Review". In: *Current Medical Imaging* 7.4 (2011), pp. 328–339. ISSN: 1573-4056/1875-6603. DOI: 10.2174/157340511798038657. URL: http://www.eurekaselect.com/article/20483.

[63] E. Ozkan, V. Vishnevsky, and O. Goksel. "Inverse problem of ultrasound beamforming with sparsity constraints and regularization". In: *IEEE Transactions on Ultrasonics, Ferroelectrics, and Frequency Control* 65.3 (2018), pp. 356–365.

[64] M.L. Palmeri et al. "A finite-element method model of soft tissue response to impulsive acoustic radiation force". In: *IEEE Transactions on Ultrasonics, Ferroelectrics, and Frequency Control* 52.10 (2005), pp. 1699–1712. DOI: 10.1109/TUFFC.2005.1561624.

[65] Mark L. Palmeri et al. "Dynamic mechanical response of elastic spherical inclusions to impulsive acoustic radiation force excitation". In: *IEEE Transactions on Ultrasonics, Ferroelectrics, and Frequency Control* 53.11 (2006), pp. 2065–2079. DOI: 10.1109/TUFFC.2006.146.

[66] Kevin J Parker. "Ultrasonic attenuation and absorption in liver tissue". In: *Ultrasound in medicine & biology* 9.4 (1983), pp. 363–369.

[67] Kevin J. Parker. "Correspondence: Apodization and Windowing Functions". In: *IEEE Transactions on Ultrasonics, Ferroelectrics, and Frequency Control* 60.6 (2013), pp. 1263–1271. DOI: 10.1109/TUFFC.2013.2691.

[68] Karl Pearson. "LIII. On lines and planes of closest fit to systems of points in space". In: *The London, Edinburgh, and Dublin Philosophical Magazine and Journal of Science* 2.11 (1901), pp. 559–572. DOI: 10.1080/14786440109462720. eprint: https://doi.org/10.1080/14786440109462720. URL: https://doi.org/10.1080/14786440109462720.

[69] Yongqiang Qiu et al. "Piezoelectric Micromachined Ultrasound Transducer (PMUT) Arrays for Integrated Sensing, Actuation and Imaging". In: *Sensors* 15.4 (2015), pp. 8020–8041. ISSN: 1424-8220. DOI: 10.3390/s150408020. URL: https://www.mdpi.com/1424-8220/15/4/8020.

[70] C. Razzetta, M. Crocco, and F. Benvenuto. *A stochastic approach to delays optimization for narrowband transmit beam pattern in medical ultrasound*. 2023. arXiv: 2209.05758 [math.OC].

[71] C. Razzetta, M. Crocco, and F. Benvenuto. *parallel parametric UltraSound Transmission software (parUST) (version v1: 2023-05-29), GitHub: https://github.com/chiararazzetta/parUST*. 2023. URL: https://github.com/chiararazzetta/parUST.

[72] Chiara Razzetta et al. “A hybrid time-frequency parametric modelling of medical ultrasound signal transmission”. In: *Advances in Computational Science and Engineering* 1.3 (2023), pp. 249–270.

[73] Ned C Rouze et al. “Parameters affecting the resolution and accuracy of 2-D quantitative shear wave images”. In: *IEEE transactions on ultrasonics, ferroelectrics, and frequency control* 59.8 (2012), pp. 1729–1740.

[74] H. Rivaz S. Goudarzi A. Basarab. “A Unifying Approach to Inverse Problems of Ultrasound Beamforming and Deconvolution”. In: *https://arxiv.org/pdf/2112.14294.pdf* (2022).

[75] A.S. Savoia, Giosue Caliano, and Massimo Pappalardo. “A CMUT probe for medical ultrasonography: from microfabrication to system integration”. In: *IEEE Transactions on Ultrasonics, Ferroelectrics, and Frequency Control* 59.6 (2012), pp. 1127–1138. DOI: 10.1109/TUFFC.2012.2303.

[76] Alessandro S. Savoia et al. “Design, Fabrication, Characterization, and System Integration of a 1-D PMUT Array for Medical Ultrasound Imaging”. In: *2021 IEEE International Ultrasonics Symposium (IUS)*. 2021, pp. 1–3. DOI: 10.1109/IUS52206.2021.9593751.

[77] Alessandro Stuart Savoia et al. “Nonlinear ultrasound imaging experiments using a CMUT probe”. In: *2016 IEEE International Ultrasonics Symposium (IUS)*. 2016, pp. 1–4. DOI: 10.1109/ULTSYM.2016.7728699.

[78] Jian Shen and Emad S. Ebbini. “A new coded-excitation ultrasound imaging system-part II: Operator design”. In: *IEEE Transactions on Ultrasonics, Ferroelectrics, and Frequency Control* 43.1 (1996). Cited by: 14, pp. 141–148. DOI: 10.1109/58.484473. URL: https://www.scopus.com/inward/record.uri?eid=2-s2.0-0029735578&doi=10.1109%2f58.484473&partnerID=40&md5=3bd8e55c2cf7d56a45d72b692186249d.

[79] Jun Shen. “Use of Amplitude and Frequency Transformations to Generate Adiabatic Pulses of Wide Bandwidth and Low RF Power Deposition”. In: *Journal of Magnetic Resonance, Series B* 112.2 (1996), pp. 131–140. ISSN:

1064-1866. DOI: https://doi.org/10.1006/jmrb.1996.0123. URL: https://www.sciencedirect.com/science/article/pii/S1064186696901235.

[80] John William Strutt. "On the Light from the Sky, its Polarization and Colour". In: *Scientific Papers*. Vol. 1. Cambridge Library Collection - Mathematics. Cambridge University Press, 2009, pp. 87–103. DOI: 10.1017/CBO9780511703966.009.

[81] Alessandro Stuart Savoia et al. "A 256-Element Spiral CMUT Array with Integrated Analog Front End and Transmit Beamforming Circuits". In: *2018 IEEE International Ultrasonics Symposium (IUS)*. 2018, pp. 206–212. DOI: 10.1109/ULTSYM.2018.8579867.

[82] Thomas L Szabo. *Diagnostic ultrasound imaging: inside out*. Academic press, 2004.

[83] T. Szasz, A. Basarab, and D. Kouamé. "Beamforming Through Regularized Inverse Problems in Ultrasound Medical Imaging". In: *IEEE Transactions on Ultrasonics, Ferroelectrics, and Frequency Control* 63.12 (2016), pp. 2031–2044. DOI: 10.1109/TUFFC.2016.2608939.

[84] M. Tanter and M. Fink. "Ultrafast imaging in biomedical ultrasound". In: *IEEE transactions on ultrasonics, ferroelectrics, and frequency control* 61.1 (2014), pp. 102–119.

[85] Radha Thangaraj et al. "Modified particle swarm optimization with time varying velocity vector". In: *International Journal of Innovative Computing, Information and Control* 8.1 (2012), pp. 201–218.

[86] N.M. Tole, H. Ostensen, and W.H.O.D.I.L. Technology. *Basic Physics of Ultrasonographic Imaging*. Who/Diagnostic Imaging and Laboratory Technology Series. World Health Organization, 2005. ISBN: 9789241592994. URL: https://books.google.it/books?id=nHnTOfxsM9cC.

[87] Piero Tortoli and Joergen Arendt Jensen. "Introduction to the Special Issue on Novel Equipment for Ultrasound Research". In: *IEEE Transactions on Ultrasonics, Ferroelectrics, and Frequency Control* 53.10 (2006), pp. 1705–1706. DOI: 10.1109/TUFFC.2006.103.

[88] B. E. Treeby and B. T. Cox. "k-Wave: MATLAB toolbox for the simulation and reconstruction of photoacoustic wave fields". In: *Journal of Biomedical Optics* 15.2 (2010), p. 021314. DOI: 10.1117/1.3360308.

[89] Andrea Trucco. "A stochastic approach to optimise wide-band beam patterns". In: *Acoustical Imaging*. Springer, 2002, pp. 123–130.

[90] C. Udriste. *Convex functions and optimization methods on Riemannian manifolds*. Springer Netherlands, 1994. DOI: 10.1007/978-94-015-8390-9. URL: https://link.springer.com/book/10.1007/978-94-015-8390-9.

[91] Pradnya A. Vikhar. "Evolutionary algorithms: A critical review and its future prospects". In: *2016 International Conference on Global Trends in Signal Processing, Information Computing and Communication (ICGTSPICC)*. 2016, pp. 261–265. DOI: 10.1109/ICGTSPICC.2016.7955308.

[92] A. I. Villalba, T. Landry, and J. Brown. "Parallel computing using Python-based software for a high-frequency ultrasound system". In: *The Journal of the Acoustical Society of America* 146.4 (Oct. 2019), pp. 3073–3073. DOI: 10.1121/1.5137663. URL: https://doi.org/10.1121/1.5137663.

[93] Peter Neil Temple Wells. "Advances in ultrasound techniques and instrumentation". In: *(No Title)* (1993).

[94] John J Wild. "The use of ultrasonic pulses for the measurement of biologic tissues and the detection of tissue density changes". In: *Surgery* 27.2 (1950), pp. 183–188.

[95] Zhao Xinchao. "A perturbed particle swarm algorithm for numerical optimization". In: *Applied Soft Computing* 10.1 (2010), pp. 119–124. ISSN: 1568-4946. DOI: https://doi.org/10.1016/j.asoc.2009.06.010. URL: https://www.sciencedirect.com/science/article/pii/S1568494609000830.

[96] Bei Yu et al. "3-D ultrasonic image reconstruction in frequency domain using a virtual transducer model". In: *Ultrasonics* 118 (2022), p. 106573. ISSN: 0041-624X. DOI: https://doi.org/10.1016/j.ultras.2021.106573. URL: https://www.sciencedirect.com/science/article/pii/S0041624X21001992.

[97] Zhi-Hui Zhan et al. "Adaptive Particle Swarm Optimization". In: *IEEE Transactions on Systems, Man, and Cybernetics, Part B (Cybernetics)* 39.6 (2009), pp. 1362–1381. DOI: 10.1109/TSMCB.2009.2015956.

[98] Dong Z. Zhang Y. Wang S., Ji G. Phillip P., and Yang j. "Pathological Brain Detection in Magnetic Resonance Imaging Scanning by Wavelet Entropy and Hybridization of Biogeography-Based Optimization and Particle Swarm Optimization". In: *Progress In Electromagnetics Research* (2015). DOI: 10.2528/PIER15040602.

[99] Heng Zhao et al. "Bias observed in time-of-flight shear wave speed measurements using radiation force of a focused ultrasound beam". In: *Ultrasound in medicine & biology* 37.11 (2011), pp. 1884–1892.